3-3-2022

Deficiency in Lyst function leads to accumulation of secreted proteases and reduced retinal adhesion.

Xiaojie Ji

Lihong Zhao

Ankita Umapathy

Bernie Fitzmaurice

Jieping Wang

See next page for additional authors

Authors

Xiaojie Ji, Lihong Zhao, Ankita Umapathy, Bernie Fitzmaurice, Jieping Wang, David S Williams, Bo Chang, Juergen K. Naggert, and Patsy M. Nishina

PLOS ONE

RESEARCH ARTICLE

Deficiency in *Lyst* function leads to accumulation of secreted proteases and reduced retinal adhesion

Xiaojie Ji[1,2], Lihong Zhao[1], Ankita Umapathy[3], Bernard Fitzmaurice[1], Jieping Wang[1], David S. Williams[3,4,5,6], Bo Chang[1], Jürgen K. Naggert[1]*, Patsy M. Nishina[1]*

1 The Jackson Laboratory, Bar Harbor, ME, United States of America, **2** Graduate School of Biomedical Science and Engineering, University of Maine, Orono, ME, United States of America, **3** Department of Ophthalmology and Stein Eye Institute, University of California, Los Angeles, CA, United States of America, **4** Department of Neurobiology, David Geffen School of Medicine, UCLA, Los Angeles, CA, United States of America, **5** Molecular Biology Institute, UCLA, Los Angeles, CA, United States of America, **6** Brain Research Institute, UCLA, Los Angeles, CA, United States of America

* Juergen.Naggert@jax.org (JKN); Patsy.Nishina@jax.org (PMN)

Citation: Ji X, Zhao L, Umapathy A, Fitzmaurice B, Wang J, Williams DS, et al. (2022) Deficiency in *Lyst* function leads to accumulation of secreted proteases and reduced retinal adhesion. PLoS ONE 17(3): e0254469. https://doi.org/10.1371/journal.pone.0254469

Editor: Olaf Strauß, Eye Hospital, Charité, GERMANY

Received: June 16, 2021

Accepted: February 18, 2022

Published: March 3, 2022

Data Availability Statement: All relevant data are within the manuscript and its Supporting Information files.

Funding: This work is supported by NIH Grant EY011996 and EY027860 to P.M.N., and EY019943 to B.C. The Jackson Laboratory Scientific Services is supported by NIH Grant CA034196. Partial funding from R01EY027442 and core grant P30EY000331 (to D.S.W.) is acknowledged. The funders had no role in study

Abstract

Chediak–Higashi syndrome, caused by mutations in the Lysosome Trafficking Regulator (*Lyst*) gene, is a recessive hypopigmentation disorder characterized by albinism, neuropathies, neurodegeneration, and defective immune responses, with enlargement of lysosomes and lysosome-related organelles. Although recent studies have suggested that *Lyst* mutations impair the regulation of sizes of lysosome and lysosome-related organelle, the underlying pathogenic mechanism of Chediak–Higashi syndrome is still unclear. Here we show striking evidence that deficiency in LYST protein function leads to accumulation of photoreceptor outer segment phagosomes in retinal pigment epithelial cells, and reduces adhesion between photoreceptor outer segment and retinal pigment epithelial cells in a mouse model of Chediak–Higashi syndrome. In addition, we observe elevated levels of cathepsins, matrix metallopeptidase (MMP) 3 and oxidative stress markers in the retinal pigment epithelium of *Lyst* mutants. Previous reports showed that impaired degradation of photoreceptor outer segment phagosomes causes elevated oxidative stress, which could consequently lead to increases of cysteine cathepsins and MMPs in the extracellular matrix. Taken together, we conclude that the loss of LYST function causes accumulation of phagosomes in the retinal pigment epithelium and elevation of several extracellular matrix-remodeling proteases through oxidative stress, which may, in turn, reduce retinal adhesion. Our work reveals previously unreported pathogenic events in the retinal pigment epithelium caused by *Lyst* deficiency. The same pathogenic events may be conserved in other professional phagocytic cells, such as macrophages in the immune system, contributing to overall Chediak–Higashi syndrome pathology.

Introduction

Chediak–Higashi syndrome (CHS) is a rare autosomal recessive disease characterized by albinism of the skin and hair, as well as hypopigmentation of the eye and additional eye pathologies including photophobia and macular hypoplasia associated with decreased visual acuity

design, data collection and analysis, decision to publish, or preparation of the manuscript.

Competing interests: The authors declare no conflict of interest.

[1–4]. Patients also display progressive neurologic dysfunction, including motor and sensory neuropathies, ataxia, and progressive neurodegeneration [1,2,5–9]. The most detrimental pathology is, however, recurrent bacterial infections, which predominantly affect the respiratory tract, skin, and mucous membranes. These infections are due to the dysfunction of polymorphonuclear leukocytes [1,2,10,11]. The majority of CHS cases progress to a life-threatening lymphoproliferative accelerated phase characterized by massive hemophagocytic lymphohistiocytosis after exposure to Epstein-Barr virus [2]. Antibiotic treatments and hematopoietic stem cell transplantation have been used to combat recurrent infections and immunological complications; but these treatments target the symptoms, not the underlying pathogenic mechanism(s) [1,2,12].

CHS is caused by mutations in the ubiquitously expressed Lysosome Trafficking Regulator (*Lyst*) gene, which encodes LYST, a Beige and Chediak-Higashi (BEACH) domain-containing protein [12–15]. The loss of LYST function results in enlarged lysosomes and lysosome-related organelles (LROs) in all cell types examined [1,14,16–22]. Functional studies using several model organisms have previously led to two distinct hypotheses for the effects of LYST in the regulation of LRO sizes: LYST may restrict homotypic lysosome fusion [23–28] by inhibiting membrane docking and fusion [23], or alternatively, LYST may promote lysosome fission [17,29,30]. However, a recent report indicates that LYST function is likely to be far more complex than a simple role in either lysosomal fusion or fission, and suggests that LYST may regulate fusion through fission-mediated recycling of the fusion machinery during lysosomal maturation [31]. Despite years of research, the exact molecular function of LYST remains unclear. Given that LYST is an extremely large protein, approximately 430 kDa in size, and contains multiple WD40 domains implicated in protein-protein interaction, it is likely that LYST has many alternate functions that are dictated by its interaction with binding partners. Thus, loss of LYST function may cause various cellular defects that have yet to be elucidated.

In this study, we examined the downstream effects of LYST dysfunction on the cellular pathology of the retinal pigment epithelium (RPE). The RPE is a monolayer of post-mitotic polarized epithelial cells, situated between the photoreceptors and the choroid; it is the primary caretaker of photoreceptor health and function [32]. One of the primary functions of the RPE is to engulf and degrade the distal tips of photoreceptor outer segments (POSs) [33,34]. Because each RPE cell serves many photoreceptor cells (200 in the mouse central retina) [35], they are tasked with degrading extraordinary amounts of POS material on a daily cycle [36,37].

By taking advantage of a novel mutant mouse strain bearing a mutation in *Lyst*, $Lyst^{bg\text{-}18J}$. We found that, in addition to enlarged and redistributed lysosomes and accumulation of phagosomes in RPE cells, there is reduced adhesion between the RPE and the neural retina. We show that the accumulation of phagosomes is associated with increased oxidative stress and an elevation of a group of proteases, including cathepsins B, L, and S, and matrix metalloprotease 3 (MMP3), which are likely secreted into the interphotoreceptor matrix (IPM) and may contribute to the retinal adhesion defect. The disturbances in lysosomal enzymatic activities may have a profound impact on tissue integrity beyond the RPE. The same mechanism is likely to also exist in the immune system, where elevation of secreted proteases that cleave cell surface proteins, potentially leads to the reduced immune response observed in CHS [38]. Our results establish a series of events for the pathogenic mechanism of CHS and suggests an important new entry point for therapeutic intervention.

Materials and methods

Mice

The *Lyst* mutant *bg-18* ($Lyst^{bg\text{-}18J}$) was first identified by the JAX Mouse Mutant Resource as a spontaneous mutation, *nm2144*. Experimental animals were housed in the same mouse room

and under the same 14-hr light/10-hr dark cycle from birth. The light cycle was 6AM to 8PM. All experiments were approved by the Institutional Animal Care and Use Committee and conducted in accordance with the ARVO Statement for the Use of Animals in Ophthalmic and Vision Research. All experiments involving mice were performed with a minimum of three pairs of sex- and age-matched wild type and mutant mice. Specific numbers of mice used for experiments are also listed in figure legends.

Indirect ophthalmoscopy, optical coherence tomography and electroretinography

Indirect ophthalmoscopy, optical coherence tomography (OCT) and electroretinography (ERG) were performed as described [39]. For indirect ophthalmoscopy and OCT, eleven 10-week-old wild type C57BL/6J male and two female mice, and four 17-week-old mutant male mice, and eleven 19-month-old male mice were used. Mouse eyes were dilated with 1% atropine ophthalmic drops (Bausch and Lomb Pharmaceuticals, Inc.) and were evaluated by indirect ophthalmoscopy with a 78-diopter lens. Fundus photographs were taken with a Micron III in vivo bright-field retinal imaging microscope equipped with image-guided OCT capabilities (Phoenix Laboratories, Inc.).

Three wild type and three mutant 2-month-old male mice were used for ERG. Electroretinograms (ERGs) were recorded from mice that were dark-adapted overnight before anesthesia with an intraperitoneal injection of xylazine (80 mg/kg) and ketamine (16 mg/kg) in normal saline solution. Recordings were done on anesthetized mice on a temperature-controlled heating pad kept at 37˚C. Dark-adapted, rod-mediated ERGs were recorded with the responses to short-wavelength flashes over 4.0-log units to the maximum intensity by the photopic stimulator. Cone-mediated ERGs were recorded with white flashes after 10 minutes of complete light adaptation. The signals were sampled at 0.8-ms intervals and averaged.

There was no unanticipated adverse event when indirect ophthalmoscopy, OCT and ERG were performed on the mice.

RNA preparation and reverse transcription

After carbon dioxide (CO_2)-induced euthanasia, mouse eyes were dissected in DEPC-treated water. The posterior eyecup was separated from connective tissues and the iris epithelium, cornea, and lens. For RPE only RNA preparations, the RPE was peeled from the neuroretina. RPE from both eyes of each animal was pooled. Poly A+ RNA from the RPE was extracted using Dynabead mRNA DIRECT Micro Kit (Invitrogen) according to the manufacturer's instructions. RNA concentration was quantified using a NanoDrop ND-1000 Spectrophotometer (NanoDrop Technologies). cDNA was synthesized using the RETROscript Kit (ThermoFisher Scientific).

Quantitative real-time PCR

Real-time PCR was performed using Bio-Rad iTaq mixture on Bio-Rad iCycler 96 thermocycler equipped with a CCD image detector, using protocols with a melt curve analysis. Only primers generating a solid major peak without obvious minor peaks in the melting curve were used. Samples were collected from three wild type and three homozygous *bg-18* mice. Each sample was subjected to three technical replications. Primers, PCR procedure and data analysis are described in detail in Supporting Information. PCR products were resolved by Metaphor agarose gel electrophoresis to confirm the expected sizes.

Western blot analysis

After mice were euthanized by CO_2 asphyxiation, the eyes were dissected in ice-cold 1X Phosphate-Buffered Saline (PBS). Individual eyecups or pooled RPE from the same animal were homogenized in ice-cold RIPA buffer [50 mM Tris.HCl pH 8.0, 1 mM EDTA, 150 mM NaCl, 1% NP-40, 0.1% SDS, and 0.5% sodium deoxycholate], freshly supplemented with phosphatase inhibitors and protease inhibitors [100 mM sodium orthovanadate, 10 mM ammonium molybdate, 0.2M sodium pyrophosphate, 1 M sodium fluoride, 0.1 M phenylmethanesulfonyl fluoride and 1% of protease inhibitor cocktails (EMD Millipore)]. Insoluble material from the lysate was removed by centrifugation for 10 minutes at 10,000 x g at 4˚C. Protein concentration was measured with Assay-free Card (EMD Millipore) and Bradford Ultra (Expedeon) kits. Equal amounts of total protein representing ~10% of the whole eyecup were used for western blot analysis as described [39]. Results were quantified using Fiji software (https://fiji.sc/).

Antibodies against phospho-MERTK (FabGennix, PMKT-140AP, rabbit polyclonal, 1:750), 4-HNE (Abcam, ab46545, rabbit polyclonal, 1:500), Glial Fibrillary Acidic Protein (GFAP, DAKO, Z0334, rabbit polyclonal, 1:1000), glyceraldehyde 3-phosphate dehydrogenase (GAPDH, Cell Signaling, 2118, rabbit monoclonal, 1:1000), phospho-ERM (Cell Signaling, 3726T, rabbit monoclonal, 1:1000), cathepsin B (Cell Signaling, 31718T, rabbit monoclonal, 1:1000), and α-tubulin (Santa Cruz, sc-53030, rat monoclonal, 1:1000) were used.

Quantification of melanin

After lysis of tissue samples with RIPA buffer, melanosomes precipitate in the insoluble pellet. The insoluble pellet was dissolved in 1 N NaOH at 80˚C for 2 hr. Absorbance of commercial melanin pigment (Sigma) at defined concentrations was measured at 405nm to establish a standard curve. The melanin content of each sample was assessed at O.D. 405 and compared to the standard curve. The pigment concentration was normalized to the total protein concentration within each sample (μg melanin/mg protein).

Retinal adhesion assay

Retinal adhesion assays were performed at two time points, 9:00 AM (3 hours after onset of the light cycle) and 3:00 PM (9 hours after onset of the light cycle). Three wild type and three mutant 7-week-old mice were used for each time point. Enucleated eyes were submerged in 20 mM HEPES-buffered Hanks' saline solution containing calcium and magnesium (Mediatech, Inc., A Corning Subsidiary) at room temperature to preserve retinal adhesion. Eyecups were dissected as described above. A single radial cut toward the optic nerve was made to flatten the eyecups. The neural retina was slowly peeled from the underlying RPE and sclera with forceps from one side of the cut edge to the other. The peeled-off neural retina was then flattened, facing upward on a glass slide for imaging.

The imaging results were confirmed with western blot analysis, which measured the amount of RPE-specific proteins in the peeled-off neural retina. Blots were incubated with primary antibodies against ezrin (Cell Signaling, 3145, rabbit polyclonal, 1:1000), GFAP, and GAPDH. Ezrin, a marker for RPE apical microvilli, was used to detect the amount of RPE attached to neural retina after separation from the RPE. GFAP and GAPDH were used as loading controls.

Transmission electron microscopy

Mice were perfused intracardially with buffered 1.2% (wt/vol) paraformaldehyde and 0.8% glutaraldehyde, and eyecups were processed using a standard procedure as described previously

[40]. The eyes for ultrastructural analyses were fixed in an ice-cold fixative solution for 3 h. The anterior segment was removed and the posterior segment cut into 1 × 2 mm blocks. Additional fixation with 0.25% glutaraldehyde/0.2% paraform- aldehyde fixative was performed for 2–8 h followed by post-fixation with 1% osmium tetroxide. The dehydrated blocks were embedded in plastic. Tissue sections were cut and stained with uranyl acetate and lead citrate and examined with a JEM-1230 transmission electron microscope (JEOL, Ltd).

Immunohistochemistry (IHC)

After mice were sacrificed by CO_2 asphyxiation, eyes were enucleated and submerged in ice-cold 4% paraformaldehyde (PFA) in PBS or acetic acid/methanol/PBS (1:3:4) overnight. Standard IHC was conducted as described [39]. Antibodies against rhodopsin (RET-P1; Thermo Fisher Scientific, MS-1233-R7, dilute each drop to 250 μL), ezrin (Cell Signaling, 3145, rabbit polyclonal, 1:200), ezrin (Santa Cruz, sc-6409, 1:200), and cathepsin B (Cell Signaling, 31718T, rabbit monoclonal, 1:200) were used. These antibodies detected bands of expected or reported sizes on western blot analyses.

Immunostaining of RPE flat mounts

Enucleated eyes were submerged in ice-cold 1X PBS and dissected as described above. The neural retina was separated from the RPE-choroid-sclera. The isolated RPE-choroid-sclera was fixed for 30 minutes in 4% PFA. Subsequently, the tissue was washed three times with 1X PBS, permeabilized with PBST (PBS with 0.1% Tween-20) for 20 minutes, and blocked with 5% donkey serum in PBST for 1 hr. Tissues were incubated with primary antibodies against rhodopsin (RET-P1; Thermo Fisher Scientific, MS-1233-R7, dilute each drop to 250 μL) and ZO-1 (Life Technologies, 61–7300, 1:200) in blocking solution overnight at 4˚C, washed with PBST, and incubated with fluorophore-conjugated secondary antibodies for 2 hr at room temperature. Nuclei were counterstained by incubating with DAPI for 20 minutes. The whole RPE-choroid-sclera tissue was then flat mounted, with the RPE side up, onto slides and with coverslips for imaging. Fluorescent images were captured with a Leica SP5 confocal microscope (Leica Microsystems), and identical imaging parameters were applied to both wild type and $Lyst^{bg\text{-}18}$ mutant RPE flat mounts.

For image analysis, only rhodopsin-positive POS fragments with diameter 0.5 μm-2.5 μm were counted by using the Imaris 9.1 software (Bitplane USA, Concord, MA, USA), with the aid of the 'Surfaces' rendering tool. Clustered POS fragments whose boundaries were difficult to delineate or those that clearly appeared to be cell surface adherent POS were not included in counts. The results were quantified and analyzed using unpaired *t*-test with Prism 6 software.

Results

Pathogenic effects of *Lyst* deficiency in the RPE

We have identified a new mutant mouse *bg-18* (B6.Cg-$Lyst^{bg\text{-}18J}$/Boc, JR#028230, The Jackson Laboratory) that recapitulates many of the pathologies observed in human CHS patients and resembles the *beige* ($Lyst^{bg\text{-}J}$) mutant previously reported [22]. Homozygous *bg-18* mutant mice, like *beige* mutant mice, display a dark grey coat color on the C57BL/6J background, compared with wild type littermates (Fig 1A). The underlying mutation was first inferred as a mutation in *Lyst* in a whole exome sequencing project on 91 mutant mice [41]. Subsequent genome mapping, complementation test with the *beige* mutant, and sequencing of *Lyst* cDNA and genomic DNA from the *bg-18* mutant definitively placed the causal mutation in the *Lyst* locus, as an intronic mutation causing a skipping of exon 10 resulting in a frameshift of the

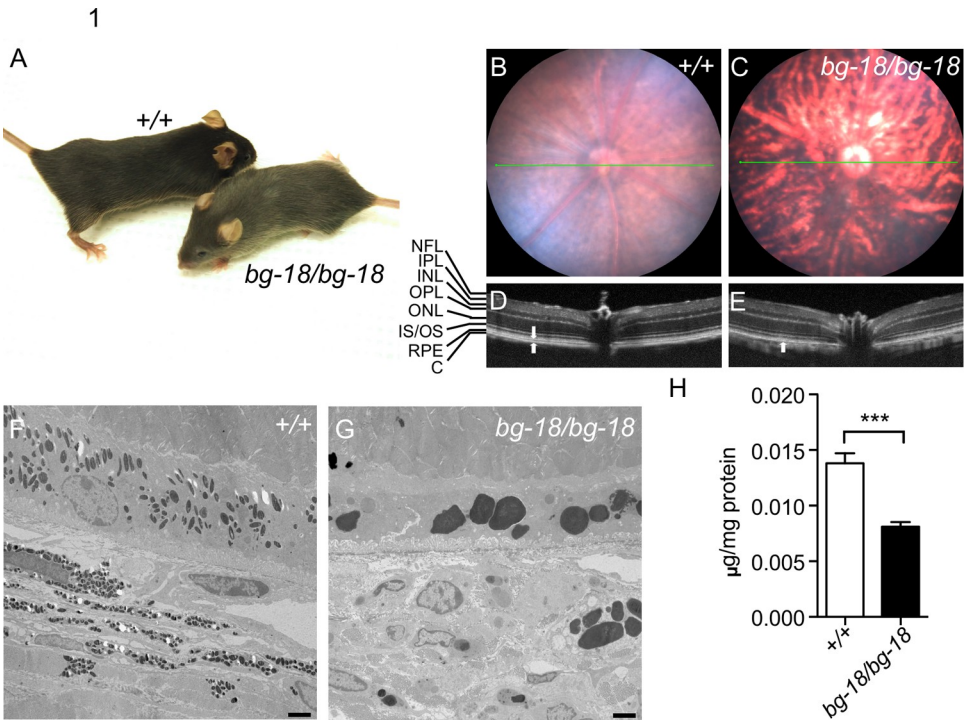

Fig 1. The clinical and pathological effects of the *bg-18* mutation on mouse retina. (A) 5-week-old wild type (+/+) and *bg-18/bg-18* mutant littermates on the C57BL/6J background. Note the lighter coat color of the *bg-18* mutant. (B-E) Abnormalities of pigmentation and reflective properties in the *bg-18* mutant retina. Fundus (B, C) and OCT (D, E) images of wild type (B, D) and *bg-18* mutant (C, E) retinas from 4-month-old mice. Retinal layers are labeled to the left. NFL: Neurofilament layer; IPL: Inner plexiform layer; INL: Inner nuclear layer; OPL: Outer plexiform layer; ONL: Outer nuclear layer; IS/OS: Inner segment/outer segment; RPE: Retina pigment epithelium; C: Choroid. Note that there are two hyper-reflective layers in the wild type retina at the location of RPE and choroid (arrows), whereas only one layer is detected in the mutant retina (arrow). (F-G) Electron micrographs of retinas from the 11-week-old wild type (F) and *bg-18* mutant (G) retinas. Scale bar = 2µm. Three mice of each genotype were examined. (H) Melanin level is reduced in the *bg-18* mutant retina from 5-week-old mice. ***: $p<0.001$, mean ± SD, n = 3 per cohort.

https://doi.org/10.1371/journal.pone.0254469.g001

mRNA and truncation of the encoded LYST protein (S1 Fig). Details describing the genetic studies are included in the Supporting Text in S1 File. We will refer to the *bg-18J* mutants as *Lyst* mutant mice, hereafter. This mutant was used to study the pathogenic effects of *Lyst* deficiency in this report.

The fundus images of homozygous *Lyst* mutants show an uneven distribution of retinal pigmentation compared to those of wild type mice (Fig 1B and 1C). Optical coherence tomography (OCT) reveals two hyper-reflective layers corresponding to the RPE and choroid in the wild type retina, while only one layer is observed at the same location in the mutant retina (Fig 1D and 1E), suggesting an alteration of the posterior retina.

By using transmission electron microscopy (TEM), we found that melanosomes in the RPE were remarkably enlarged both in the RPE and choroid of the *Lyst* mutants, relative to melanosomes in controls (Fig 1F and 1G). Because the melanosomes tended to aggregate without distinct boundaries (S2 Fig), we were unable to distinguish individual organelles and quantitate their number. However, a significant reduction of melanin concentration was observed in the *Lyst* mutant eyecups compared with wild type controls (Fig 1H), indicating a reduction in melanogenesis or an increase in melanin turnover.

At 2 months of age, *Lyst* mutants show similar rod and cone electroretinography (ERG) responses to wild type controls (S3 Fig), indicating no obvious electrophysiological defects or

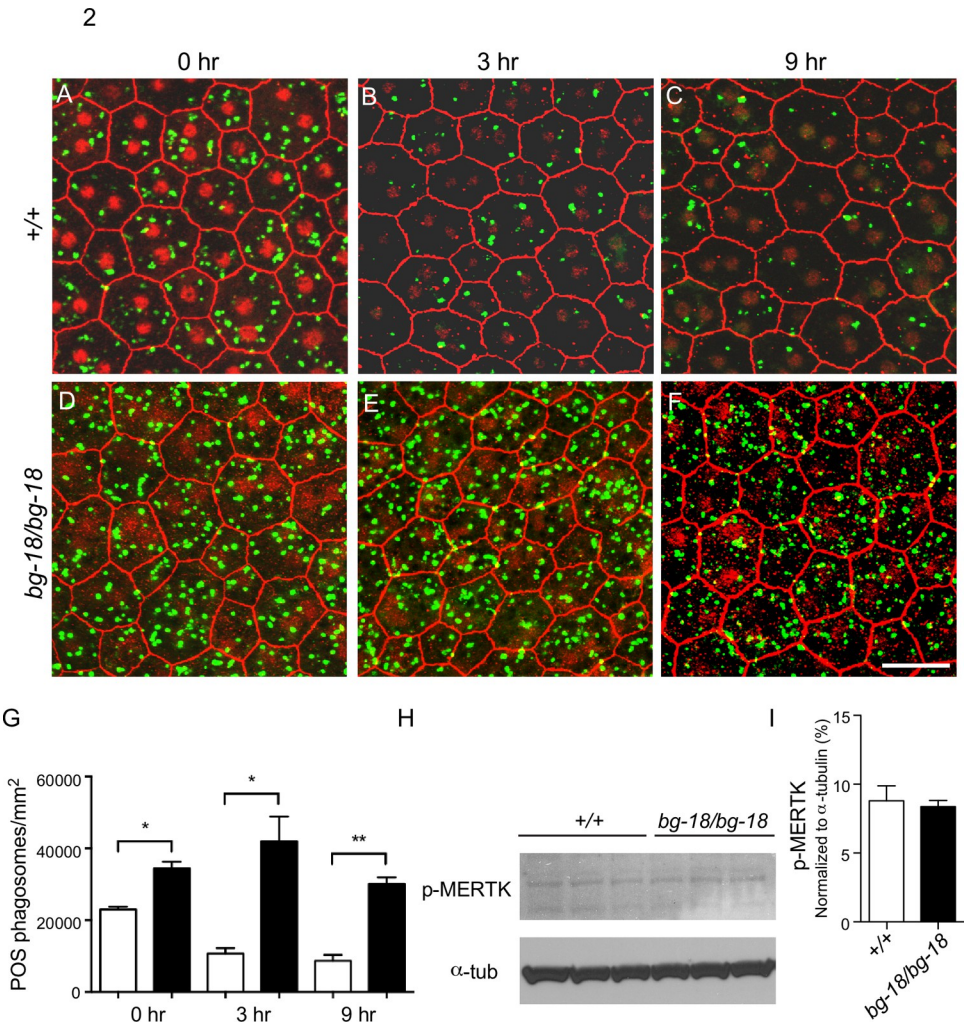

Fig 2. Accumulation of phagosomes in *bg-18* RPE cells. (A-G) Number of phagosomes in RPE from 7 to 8-week-old wild-type and *bg-18* mutant mice. Wild type (A-C) and *bg-18* mutant (D-F) RPE was incubated with antibodies against ZO-1 (red) and rhodopsin (green), after dissection at 0 (A, D), 3 (B, E), and 9 (C, F) hours after the onset of light at 6 AM. Note that the ZO-1 staining in the nuclei is an artifact of over-staining with DAPI which can result in bleed over signal into the red channel. This does not affect the green channel. Scale bar = 50μm. Images covering larger areas are shown in S6 Fig. The results were quantified and analyzed using unpaired *t*-test (G). *: P<0.05, **: P<0.01, mean ± SD, n = 3. (H-I) Ingestion of POS tips is not affected in the *bg-18* mutant RPE from 5-week-old mice, as assessed by the phospho-MERTK level using western blot analysis (H). Quantified results are shown in (I) as mean ± SD, n = 3 per cohort.

https://doi.org/10.1371/journal.pone.0254469.g002

retinal degeneration at this age. ERG measurements were also attempted on aged *Lyst* mutants but were not successful as their eyes could not be dilated. However, retinal degeneration was not observed at 19 months of age in OCT images of *Lyst* mutant eyes (S4 Fig).

Increased number of phagosomes in the *Lyst* mutant RPE. The tips of rod OS are phagocytosed by the RPE immediately after light onset [36,37]. We counted the numbers of phagosomes containing rod outer segments (OS) in RPE flat mounts from wild type and *Lyst* mutant mice at 7 to 8 weeks of age. At the time of light onset, the number of RPE phagosomes in *Lyst* mutant RPE were slightly higher compared with wild type control (Fig 2A and 2D). We also compared the numbers of RPE rhodopsin-positive phagosomes in IHC images of 5-week-old wild type and *Lyst* mutant eyes at 0.5, 1, and 2 hr after light onset and found that the

3

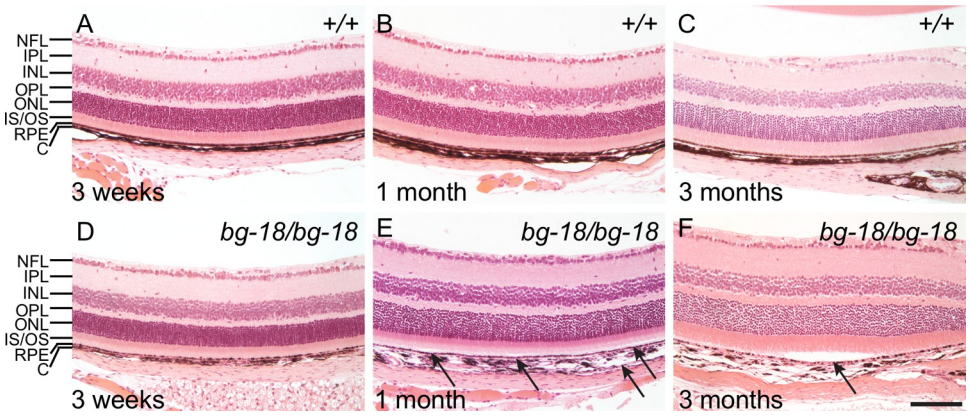

Fig 3. Progressive retinal detachment in *bg-18* mutant eyes as shown by H&E staining. Wild type (A-C) and mutant (D-F) retinas are compared at 3 weeks (A, D), 1 month (B, E), and 3 months (C, F) of age. Note the separation between the neural retina and RPE in the 1-month-old mutant eye (E) and the larger area of detachment in the retina of the 3-month-old mutant (F), marked by arrows. Retina layers are labeled as in Fig 1D. (n = 3 per cohort) Scale bar = 100μm.

https://doi.org/10.1371/journal.pone.0254469.g003

number of phagosomes were higher in the mutant RPE at all time points examined (S5 Fig). The most remarkable differences in the number of rhodopsin-positive phagosomes in *Lyst* mutant RPE cells when compared to wild type, however, was at 3 or 9 hr after light onset (Figs 2B, 2C, 2E–2G and S6).

The increase in RPE phagosomes may either be due to elevated ingestion of POS tips or reduction in lysosomal degradation of engulfed phagosomes in the RPE. To differentiate between these two possibilities, the level of active, phosphorylated MER proto-oncogene tyrosine kinase (MERTK), which is essential for ingestion of POS tips and has been reported to increase upon the onset of phagocytosis [42], was assessed by western blot analysis. No obvious change was observed right after light onset (Fig 2H and 2I), the time point of peak phagosome number reported previously [43]. As MERTK is only localized on the apical surface of the RPE cells, this result indicates that ingestion of POS tips is not affected in the RPE of *Lyst* mutants. In addition, we found that the phosphorylated MERTK was still mainly observed in the *Lyst* mutant RPE at the time of lights-on but not at later sampled time points (S5 Fig). This finding suggests that ingestion of POS tips in LYST-deficient RPE cells is not prolonged and that the main defect resulting from the *Lyst* mutation likely involves the degradation phase of this process. Our observation of an accumulation of undigested phagosomes in LYST-deficient RPE is consistent with this conclusion. Previous research has shown that the fusion between phagosomes and lysosomes is blocked by the re-distribution of lysosomes to perinuclear clusters induced by lipopolysaccharide (LPS) treatment in dendritic cells [44]. Other studies have demonstrated giant and perinuclear lysosomes in *Lyst*-deficient cells [19,45,46]. Our $Lyst^{bg\text{-}18J}$ mice recapitulate this subcellular phenotype of lysosomes (S7 Fig). It is possible that the perinuclear aggregation of lysosomes contributes to the accumulation of phagosomes in the RPE of *Lyst* mutants by blocking phago-lysosomal fusion.

Reduced retinal adhesion in LYST deficient mice

When we performed histology, and compared the wild type (Fig 3A–3C) to the 3-week-old *Lyst* mutant retinas (Fig 3D), we observed small areas of detachment of the neural retina from

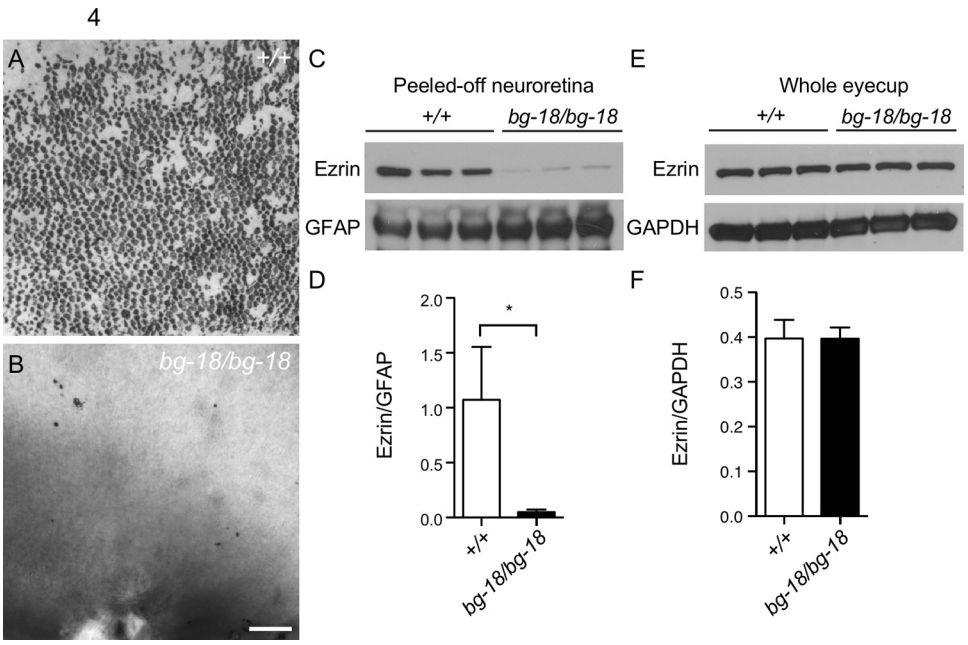

Fig 4. Reduced retinal adhesion in *Lyst* mutant mice. (A-B) Pigment remaining on peeled-off retina from 7-week-old wild type (A) and mutant (B) eyes. Scale bar = 100μm. **C-D.** Reduced ezrin level in the mutant neuroretina shown by western blot analysis (C). Quantified results are shown (D). Ezrin levels were normalized to the levels of GFAP. (E-F) Total ezrin levels are similar in mutant and wild type control eyecups in western blot analysis (E) and quantified results (F). *: $P<0.05$, mean ± SD, n = 3 per cohort.

https://doi.org/10.1371/journal.pone.0254469.g004

the RPE in sections from every homozygous *Lyst* mutant mouse examined (n>3 for each time cohort). The detachment was observed as early as 1 month of age (Fig 3E), which appeared as larger areas of detachment by 3 months of age (Fig 3F). However, retinal detachment is not observed by OCT at 1 or 3 months (S8 Fig). The detachment observed by histology may result from a meaningful artifact that occurs during enucleation of the eye and histological sample preparation due to the reduced retinal adhesion and is, therefore, not observed by OCT, which is an *in situ* technique.

Separation of the neural retina from its supportive structures can lead to significant visual defects [47–52]. The microvilli-rich apical domains of RPE cells, which form the outermost layer of the retina, interdigitate with the photoreceptor outer segments. Thus, apical domains of RPE cells or even entire RPE cells may remain attached when the neural retina is mechanically peeled from the RPE [42]. To determine if the retinal detachment observed by histology, but not by OCT, was an artifact of histological sample preparation or the consequence of reduced retinal adhesion insufficient to induce detectable retinal detachment *in vivo*, we compared the adhesion between the RPE and neuroretina in wild type and *Lyst* mutants accordingly. In the wild type peeled-off neural retina, RPE pigment was abundantly attached to the surface of photoreceptor outer segments (POS); whereas the peeled-off neural retina of the age-matched *Lyst* mutant mice (separated under the same experimental conditions and at similar times of day), were almost devoid of RPE pigment (Fig 4A and 4B). To quantify the alteration in adhesion, the level of ezrin, an RPE microvillus marker was measured by western blot analysis in the peeled-off retinas. Compared to wild type neural retina, the ezrin levels were significantly reduced in the *Lyst* mutant peeled-off neural retina (Fig 4C and 4D). In contrast, ezrin levels were similar in the wild type and mutant whole eyecups (Fig 4E and 4F). Therefore, the reduction in ezrin levels in the mutant peeled-off neural retina is likely due to poor RPE-

retina adhesion in the *Lyst* mutant mice, and not due to a decrease in ezrin levels in the RPE microvilli.

Levels of cysteine cathepsins and MMP3 are increased in the *Lyst* mutant eyecups

The POS and RPE microvilli of the *Lyst* mutant mice were not as densely packed as those in the wild type retina, but the structure of the processes were still clearly visible and comparable to that of the wild type mice (S9 Fig). In addition, we also examined ERM (ezrin, radixin, moesin) proteins that are activated upon phosphorylation (Thr567 of ezrin, Thr564 of radixin, Thr558 of moesin) and link membrane-associated proteins to actin filaments at the cell cortex, making them important for RPE microvilli morphology. No significant differences were observed in the level of phospho-ERM between wild type and *Lyst* eyecups (S9 Fig). These results suggest that the reduced adhesion between the neural retina and RPE in the mutant eye is unlikely to be due to structural alterations.

Adhesion of the neuroretina to the RPE is mediated by the interphotoreceptor matrix (IPM), a retina-specific type of extracellular matrix (ECM) between the RPE and POS. Previously, it was shown that proteases, such as matrix metalloproteinases (MMPs) and cysteine cathepsins, are found in the ECM and play important roles in ECM remodeling [53–56]. Quantitative real-time PCR showed up-regulation of transcripts of cathepsins and MMP12 in *Lyst* mutant ocular tissues [57]. To confirm previous reports and pinpoint the precise locations where the up-regulations actually occur, we tested transcripts of cathepsin B, L, and S and MMP3 in the RPE, because it appears to be the most affected layer in the retina by the *Lyst* mutation. Consistent with previous reports, we also found that the transcription levels of MMP3, and cathepsin B, L, and S assessed by quantitative real-time PCR, are increased in the RPE of the *Lyst* mutants relative to control (Fig 5A–5D). However, in both wild type and the *Lyst* mutant RPE, MMP3 and cathepsin S transcriptional expression was very low, and the protein levels, assessed by western blot analysis, were below detection level. Thus, in this study, our analysis focused on cathepsin B, as it is the most abundant cysteine protease in the RPE [58]. However, other aforementioned proteases upregulated by *Lyst* deficiency may play similar roles in the IPM.

Cathepsin B is a lysosomal cysteine protease normally found ubiquitously in cells and tissues [59]. In malignant tumors, the expression of cathepsin B is highly upregulated and mature cathepsin B is secreted to the cell surface where it can degrade ECM proteins. The degradation of ECM proteins by cathepsin B is required for tumor cell invasion and metastasis [53,55,56,60]. To test if molecular changes of cathepsin B could be responsible for the reduced adhesion between RPE and neural retina in the *Lyst* mutant eye, cathepsin B protein levels were measured by western blot analysis. In the *Lyst* mutant eyecups, a significant elevation of mature cathepsin B protein was observed (Fig 5E and 5F). Mature cathepsin B, which was mainly found in the RPE samples and not in neural retina samples, was dramatically increased relative to controls (Fig 5G). By immunohistochemical staining, a strong cathepsin B signal was observed at the apical surface of the RPE, which colocalized with ezrin (Fig 5H–5M), and juxtaposed to the rhodopsin-labeled POS (S10 Fig). Combined with the QPCR and western blot results, these results indicate that perhaps the elevated levels of mature cathepsin B on the apical surface of RPE and interfacing POS may contribute to the reduced retinal adhesion in the *Lyst* mutant mice.

The level of oxidative stress is increased in the *Lyst* mutant RPE

Previous studies have reported elevated expression levels of cysteine cathepsins in mouse RPE exposed to oxidative stress [58]. MMPs were also reported to be upregulated by oxidative stress

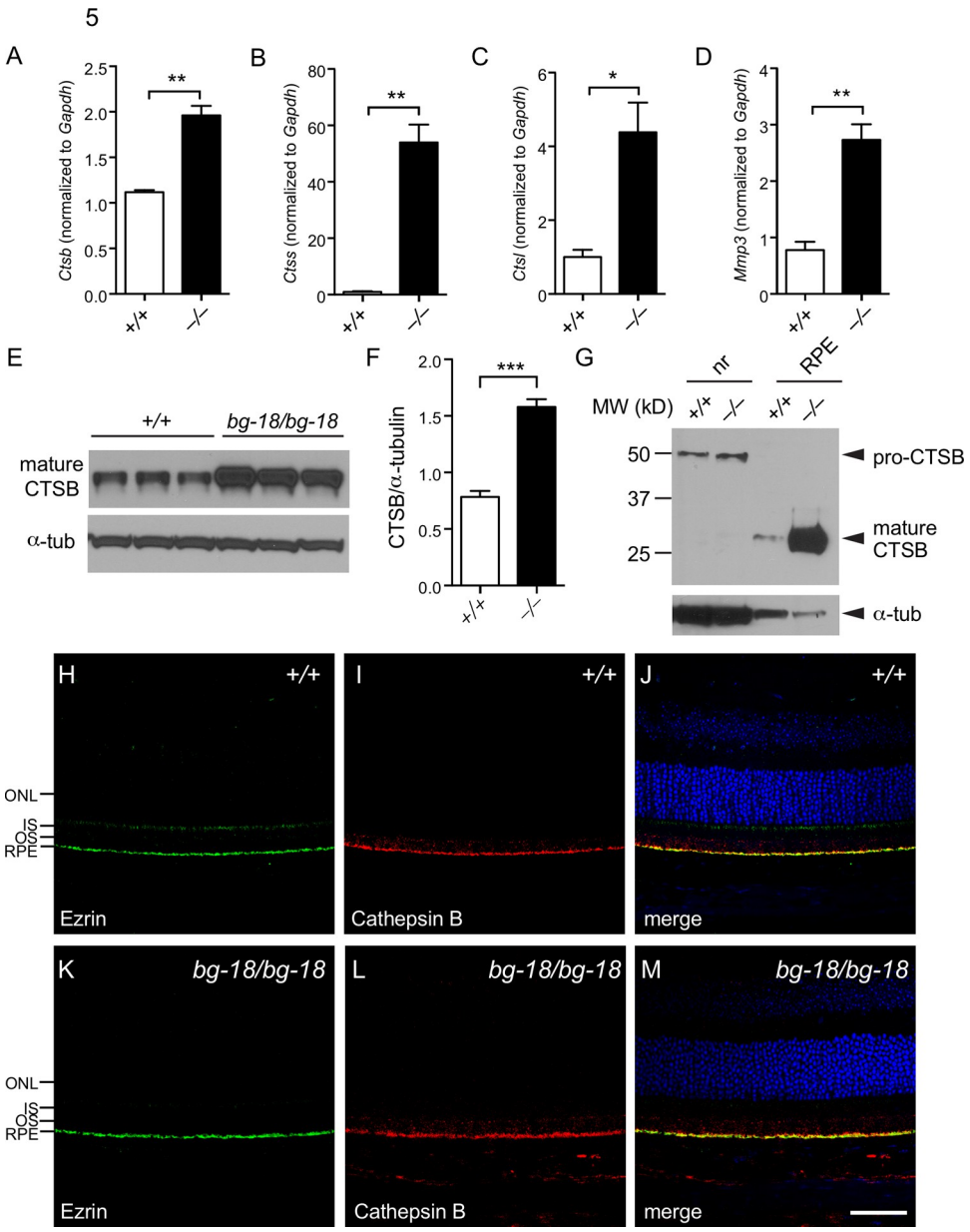

Fig 5. Elevation of cathepsins and MMP3 in the *Lyst* mutant RPE. (A-D) Quantitative RT-PCR results showing cathepsin B (A), cathepsin S (B), cathepsin L (C), and MMP3 (D) transcript levels in 3-week-old wild type (open bars) and mutant (filled bars) RPE. Three mice of each genotype and three technical replicates per mouse were used. Values are expressed as mean ± SD, *: P<0.05; **: P<0.01 (two-tail unpaired *t*-test). (E-F) Cathepsin B (CTSB) protein level is also increased in 3-week-old mutant RPE shown by western blot analysis (E). The results are quantified (F). Three mice of each genotype were used. Values are expressed as mean ± SD, n = 3, ***: P<0.001 (two-tail unpaired *t*-test). **G.** In the retina, mature cathepsin B is mainly in the RPE, whereas the pro-cathepsin in the neuroretina is largely unprocessed. (H-M) Cathepsin B is localized to the apical surface of the RPE. Retinal sections from 4-week-old wild type (H-J) and mutant (K-M) were subjected to immunohistochemistry with antibodies against ezrin (H, K) and cathepsin (I, L). Merged images are shown (J, M). (n = 3 per cohort) Retinal layers are labeled to the left. ONL: Outer nuclear layer; IS: Inner segment; OS: Outer segment; RPE: Retina pigment epithelium. Scale bar = 50μm.

https://doi.org/10.1371/journal.pone.0254469.g005

in many other cell types [61–64]. These data suggest that the observed increase in levels of cysteine cathepsins and MMP3 of *Lyst* mutant RPE cells may be caused by elevated levels of oxidative stress as well. By western analysis, we determined that the level of 4-hydroxynonenal

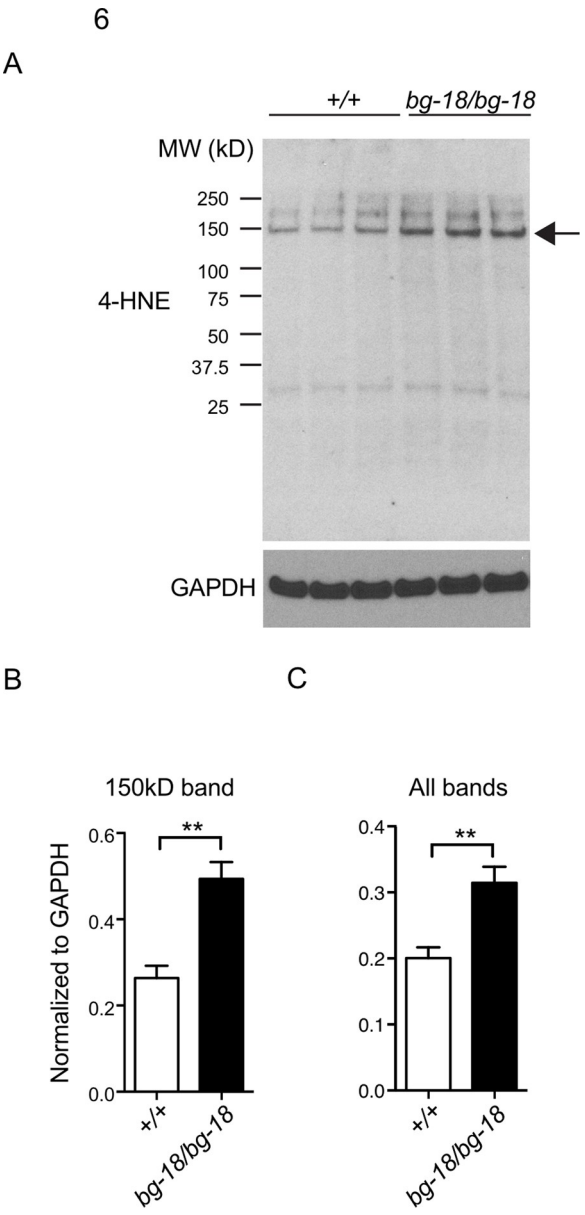

Fig 6. Increased oxidative stress in the *Lyst* mutant RPE. (A) Western blot analysis of 4-HNE modified proteins in 4-week-old wild type (+/+) and mutant (*bg-18/bg-18*) RPE, n = 3 per cohort. (B-C) The 150 kDa band on the western (A, arrow), and all bands including the 150 kDa band are quantified, respectively.

https://doi.org/10.1371/journal.pone.0254469.g006

(4-HNE)-modified protein, a widely used biomarker for oxidative stress, was increased in the *Lyst* mutant RPE cells compared to wild type control (Fig 6). Thus, we postulate that the oxidative stress due to *Lyst* deficiency results in elevation of secreted proteases in the IPM between the RPE and the photoreceptors.

Discussion

In this study, our results demonstrate for the first time that LYST plays an important role in phagosome processing in RPE cells. We observed an abnormal accumulation of phagosomes

in RPE cells in *Lyst* mutant mice (Figs 2 and S5). Previous studies have suggested that phagocytosis of photoreceptor outer segments by RPE cells causes oxidative stress. For example, long-term daily feeding of rod OS increases the number of intracellular autofluorescent granules and increases catalase activity in cultured human RPE cells [65,66], and rod OS uptake by cultured human RPE cells increases oxygen consumption and intracellular H_2O_2 production [67]. Thus, we reasoned that the accumulation of phagosomes may cause an increase in oxidative stress in the *Lyst* mutant RPE cells. In support of this hypothesis, studies have shown that slowed degradation of POS phagosomes causes oxidative stress characterized by the increase of oxidative stress markers, i.e., malondialdehyde (MDA) or 4-HNE levels, in the RPE [68,69]. Our data shows that the levels of 4-HNE-modified proteins are increased in the *Lyst* mutant RPE compared with those in the wild type control samples, indicative of oxidative stress (Fig 5). It is possible that the increased oxidative stress is in part due to the elevated oxidation of the ingested POS in the mutant RPE phagosomes because of less efficient breakdown of its oxidized contents.

Previous studies in tumor tissues suggested that oxidative stress could cause elevation of secreted cathepsin B and MMPs, which contributed to the digestion of extracellular matrix during tumor metastasis [53,55,56,60]. In addition, in a mouse model of chronic oxidative stress, termed Hyperoxia-Related Retinal Degeneration (HRRD), elevation of transcript and protein levels of cathepsin B, L, and S in the RPE have been reported [58]. Strikingly, we also observed an increase in cathepsin B, L, and S, as well as MMP3 mRNA levels in *Lyst* mutant RPE (Fig 4A–4F). Our data further showed that cathepsin B is localized to the apical surface of RPE (Fig 4H–4M), where it could potentially degrade IPM proteins and thus affect the adhesion of the neuroretina to the RPE. Increased protease activity on the RPE apical surface could promote IPM remodeling and reduce adhesion of the neuroretina to the RPE. Taken together, our results suggest that in *Lyst* mutant RPE, phagosome accumulation leads to oxidative stress, which results in increased expression of proteases on the RPE apical surface, thus reducing overall RPE-retinal adhesion. Although we observed visible retinal detachment only after mechanical stress during removal of the eye from the animal, it is known that blunt ocular trauma is a common cause for retinal detachment [70–72]. Whether the *Lyst* mutation increases the risk of retinal detachment can be explored in the future, by comparing the wild type and the *Lyst* mutant retina in the presence of mechanically induced retinal detachment using a method described previously [73].

Oxidative stress contributes to the pathogenesis of many neurodegenerative diseases including age-related macular degeneration (AMD). In addition, cathepsins have been implicated in the pathogenesis of AMD [58,74–76]. Whether oxidative stress contributes to AMD via aberrant activation of cathepsins is still unclear. Research on the regulation of cysteine cathepsins in the context of oxidative stress may provide new therapeutic targets for AMD. Thus, the *Lyst* mutant mice may be a valuable genetic model to study the impact of chronic oxidative stress on the RPE.

RPE cells are highly phagocytic, and thus examining this cell type provides a unique opportunity to study phagocytosis *in vivo*. A similar pathological pathway described here may also exist in *Lyst*-deficient leukocytes where excessive secreted cathepsin B and other secreted proteases may cleave surface antigen or receptors, thus contributing to the decreased immune response seen in CHS patients. Alternatively, *Lyst* deficiency may primarily reduce the immune response through decreased digestion of phagosomes by lysosomes in leukocytes, which is critical for antigen presentation. The exact outcome caused by phagosome accumulation-induced oxidative stress in leukocytes versus cells in tissue such as the RPE will have to be determined experimentally in the future.

Supporting information

S1 Fig. The *bg-18* mutation shown in cDNA and genomic DNA sequences. (A-B) cDNA sequences of the wild type (A) and mutant (B) around exon 10. Note the absence of exon 10 in mutant cDNA. (C) Genomic DNA sequences of the wild type (top) and mutant (bottom) around exon 10. The G to A transition is shaded in pink.
(TIF)

S2 Fig. Melanosomes in *bg-18* mutant RPE are often aggregated or fused. Arrows mark the locations of possible boundaries between melanosomes in the same cluster. Mice were 11-week-old upon euthanasia. Scale bar = 500 nm.
(TIF)

S3 Fig. The *bg-18* mutant retina display normal electroretinographic patterns at two months of age. (A-B) Representative rod (A) and cone (B) ERG of the wild type (blue) and the mutant (red) eyes. (C-E) Quantified results of the a-wave (C) and b-wave (D) of rods, and the cone b-wave response (E).
(TIF)

S4 Fig. The *bg-18* mutant retina does not display retinal degeneration. OCT images of the retina from 10-week-old wild type (+/+, A), 17-week-old mutant (B) and 19-month-old mutant mice (C). Retinal layers are labeled. NFL: Neurofilament layer; IPL: Inner plexiform layer; INL: Inner nuclear layer; OPL: Outer plexiform layer; ONL: Outer nuclear layer; IS/OS: Inner segment/outer segment; RPE: Retina pigment epithelium; C: Choroid. Note that there is only one hyper-reflective layer left at the location of RPE and choroid layers in the mutant retina (arrows). However, the overall thickness of the neuroretina is similar in the mutant eye compared with that in the wild type.
(TIF)

S5 Fig. The numbers of rhodopsin-positive phagosomes are increased in *bg-18* mutant RPE. (A-D) Representative immunohistochemical images of wild type (A, C) and mutant (B, D) retina at 0 (A, B) and 1 (C, D) hour after onset of light, stained with antibodies against ZO-1 (red) and rhodopsin (green). Retinal layers are labeled. ONL: Outer nuclear layer; RPE: Retina pigment epithelium. Note that the sizes of phagosomes in the mutant RPE appear larger in general compared with the wild type RPE. Three mice of each genotype were used for each time-point. Scale bar = 50 μm. (E) Quantified results showing the number of phagosomes in the wild type (blue) and mutant (pink) RPE at 0, 30, 60 and 120 minutes after light onset. Phagosomes from 2 equally-sized areas of each retina section were counted in samples from 3 wild type and 3 mutant mice. *: $P < 0.05$; **: $P < 0.01$. Two-tailed t-test. (F) Phospho-MERTK level was reduced after the onset of light in both the wild type and the mutant retina. Western blot analysis showing p-MERTK level at 0, 0.5 and 3 hour after light onset in the wild type (+/+) and the mutant (bg-18/bg-18) eyecups. Alpha-tubulin was used as the loading control. All mice used in this figure were 5-week-old at time of euthanasia.
(TIF)

S6 Fig. Number of phagosomes in wild-type and *bg-18* mutant RPE flat mounts. RPE from 5-week-old wild type (A-C) and *bg-18* mutant (D-F) mice was incubated with antibodies against ZO-1 (red) and rhodopsin (green), after dissection at 0 (A, D), 3 (B, E), and 9 (C, F) hours after the onset of light at 6 AM. 3 mice of each genotype were examined for each time-point. The images show single confocal z-sections. Areas circled with squares are also enlarged and shown in Fig 2.
(TIF)

S7 Fig. The morphology of lysosomes in wild type and *bg-18* mutant MEFs. Wild type (A-C) and mutant (D-F) MEFs were transiently transfected with a plasmid expressing GFP-LAMP1 (A, D), and counterstained with phalloidin (B, E). The merged images are shown in (C, F). Scale bar = 10 μm.
(TIF)

S8 Fig. Retinal detachment was not observed in the *bg-18* homozygous mutant mice by OCT. Representative OCT sections from 2-month-old wild type (A) and mutant (B) retina are shown. Each image is the average of a stack of 50 scans. Retinal layers are labeled as in S4 Fig. Note the photoreceptor outer segment (OS) layer is not detached from underlying layers. In addition, there are two hyper-reflective layers corresponding to RPE and choroid, respectively, in the wild type retina, but only one layer is observed at the same location in the mutant retina.
(TIF)

S9 Fig. Normal RPE microvilli in the *bg-18* mutant retina. (A-B) Transmission electronic micrographs of 11-week-old wild type (A) and mutant (B) retina showing the photoreceptor outer segments (POS) and RPE. Several RPE microvilli in the mutant retina are marked with arrows. Scale bar = 2 μm. (C-D) Western blot analysis (C) showing phospho-ERM in 5-week-old wild type (+/+) and homozygous mutant eye cups. The results were quantified in (D). Note the similar pERM levels after normalizing to the internal loading control GAPDH.
(TIF)

S10 Fig. Cathepsin B in the apical RPE interfaces the photoreceptor outer segment layer. Wild type (A-C) and mutant (D-F) retina sections from 4-week-old mice were subjected to immunostaining with rhodopsin (A, D) and cathepsin B (B, E). The merged results (C, F) show the localization of rhodopsin and cathepsin B layers in proximity. Retinal layers are labeled as in Fig 4. Scale bar = 50 μm.
(TIF)

S1 Raw images. Unprocessed original data for western blots used.
(PDF)

S1 File. Supporting text. Additional details of methods used for this manuscript and supporting information.
(PDF)

Acknowledgments

We thank the Sequencing, Histology and Imaging Sciences, and Multimedia Services at The Jackson Laboratory for their assistance in our studies. We also thank Ms. Melissa Berry for nomenclature review of the manuscript.

Author Contributions

Conceptualization: Xiaojie Ji, Lihong Zhao, Jürgen K. Naggert, Patsy M. Nishina.

Formal analysis: Xiaojie Ji, Lihong Zhao, Ankita Umapathy, David S. Williams.

Funding acquisition: David S. Williams, Bo Chang, Patsy M. Nishina.

Investigation: Xiaojie Ji, Lihong Zhao, Ankita Umapathy, Jieping Wang.

Methodology: Xiaojie Ji, Lihong Zhao, Ankita Umapathy, Bernard Fitzmaurice.

Resources: Bernard Fitzmaurice, Jieping Wang, Bo Chang.

Writing – original draft: Xiaojie Ji.

Writing – review & editing: Lihong Zhao, Ankita Umapathy, David S. Williams, Bo Chang, Jürgen K. Naggert, Patsy M. Nishina.

References

1. Kaplan J, De Domenico I, Ward DM. Chediak-Higashi syndrome. Curr Opin Hematol. 2008; 15(1):22–9. https://doi.org/10.1097/MOH.0b013e3282f2bcce PMID: 18043242.
2. Lozano ML, Rivera J, Sanchez-Guiu I, Vicente V. Towards the targeted management of Chediak-Higashi syndrome. Orphanet J Rare Dis. 2014; 9:132. https://doi.org/10.1186/s13023-014-0132-6 PMID: 25129365; PubMed Central PMCID: PMC4243965.
3. BenEzra D, Mengistu F, Cividalli G, Weizman Z, Merin S, Auerbach E. Chediak-Higashi syndrome: ocular findings. J Pediatr Ophthalmol Strabismus. 1980; 17(2):68–74. https://doi.org/10.3928/0191-3913-19800301-04 PMID: 7391900.
4. Valenzuela R, Morningstar WA. The ocular pigmentary disturbance of human Chediak-Higashi syndrome. A comparative light- and electron-microscopic study and review of the literature. Am J Clin Pathol. 1981; 75(4):591–6. https://doi.org/10.1093/ajcp/75.4.591 PMID: 7223721.
5. Sung JH, Stadlan EM. Neuropathological changes in Chediak-Higashi disease. J Neuropathol Exp Neurol. 1968; 27(1):156–7. PMID: 5656570.
6. Sung JH, Meyers JP, Stadlan EM, Cowen D, Wolf A. Neuropathological changes in Chediak-Higashi disease. J Neuropathol Exp Neurol. 1969; 28(1):86–118. https://doi.org/10.1097/00005072-196901000-00005 PMID: 5766368.
7. Hirano A, Zimmerman HM, Levine S, Padgett GA. Cytoplasmic inclusions in Chediak-Higashi and Wobbler mink. An electron microscopic study of the nervous system. J Neuropathol Exp Neurol. 1971; 30 (3):470–87. https://doi.org/10.1097/00005072-197107000-00011 PMID: 4327884.
8. Misra VP, King RH, Harding AE, Muddle JR, Thomas PK. Peripheral neuropathy in the Chediak-Higashi syndrome. Acta Neuropathol. 1991; 81(3):354–8. https://doi.org/10.1007/BF00305881 PMID: 2058369.
9. Tardieu M, Lacroix C, Neven B, Bordigoni P, de Saint Basile G, Blanche S, et al. Progressive neurologic dysfunctions 20 years after allogeneic bone marrow transplantation for Chediak-Higashi syndrome. Blood. 2005; 106(1):40–2. https://doi.org/10.1182/blood-2005-01-0319 PMID: 15790783.
10. Padgett GA, Reiquam CW, Henson JB, Gorham JR. Comparative studies of susceptibility to infection in the Chediak-Higashi syndrome. J Pathol Bacteriol. 1968; 95(2):509–22. https://doi.org/10.1002/path.1700950224 PMID: 4172085.
11. Blume RS, Wolff SM. The Chediak-Higashi syndrome: studies in four patients and a review of the literature. Medicine (Baltimore). 1972; 51(4):247–80. PMID: 5064229.
12. Cullinane AR, Schaffer AA, Huizing M. The BEACH is hot: a LYST of emerging roles for BEACH-domain containing proteins in human disease. Traffic. 2013; 14(7):749–66. https://doi.org/10.1111/tra.12069 PMID: 23521701; PubMed Central PMCID: PMC3761935.
13. Barbosa MD, Nguyen QA, Tchernev VT, Ashley JA, Detter JC, Blaydes SM, et al. Identification of the homologous beige and Chediak-Higashi syndrome genes. Nature. 1996; 382(6588):262–5. https://doi.org/10.1038/382262a0 PMID: 8717042; PubMed Central PMCID: PMC2893578.
14. Nagle DL, Karim MA, Woolf EA, Holmgren L, Bork P, Misumi DJ, et al. Identification and mutation analysis of the complete gene for Chediak-Higashi syndrome. Nat Genet. 1996; 14(3):307–11. https://doi.org/10.1038/ng1196-307 PMID: 8896560.
15. Perou CM, Moore KJ, Nagle DL, Misumi DJ, Woolf EA, McGrail SH, et al. Identification of the murine beige gene by YAC complementation and positional cloning. Nat Genet. 1996; 13(3):303–8. https://doi.org/10.1038/ng0796-303 PMID: 8673129.
16. Ward DM, Griffiths GM, Stinchcombe JC, Kaplan J. Analysis of the lysosomal storage disease Chediak-Higashi syndrome. Traffic. 2000; 1(11):816–22. https://doi.org/10.1034/j.1600-0854.2000.011102.x PMID: 11208072.
17. Perou CM, Leslie JD, Green W, Li L, Ward DM, Kaplan J. The Beige/Chediak-Higashi syndrome gene encodes a widely expressed cytosolic protein. J Biol Chem. 1997; 272(47):29790–4. https://doi.org/10.1074/jbc.272.47.29790 PMID: 9368050.
18. White JG, Clawson CC. The Chediak-Higashi syndrome: ring-shaped lysomomes in circulating monocytes. Am J Pathol. 1979; 96(3):781–98. PMID: 474718; PubMed Central PMCID: PMC2042404.

19. Burkhardt JK, Wiebel FA, Hester S, Argon Y. The giant organelles in beige and Chediak-Higashi fibroblasts are derived from late endosomes and mature lysosomes. J Exp Med. 1993; 178(6):1845–56. https://doi.org/10.1084/jem.178.6.1845 PMID: 7902407; PubMed Central PMCID: PMC2191291.

20. Zhao H, Boissy YL, Abdel-Malek Z, King RA, Nordlund JJ, Boissy RE. On the analysis of the pathophysiology of Chediak-Higashi syndrome. Defects expressed by cultured melanocytes. Lab Invest. 1994; 71 (1):25–34. PMID: 8041115.

21. Introne W, Boissy RE, Gahl WA. Clinical, molecular, and cell biological aspects of Chediak-Higashi syndrome. Mol Genet Metab. 1999; 68(2):283–303. https://doi.org/10.1006/mgme.1999.2927 PMID: 10527680.

22. Ward DM, Shiflett SL, Kaplan J. Chediak-Higashi syndrome: a clinical and molecular view of a rare lysosomal storage disorder. Curr Mol Med. 2002; 2(5):469–77. https://doi.org/10.2174/1566524023362339 PMID: 12125812.

23. Tchernev VT, Mansfield TA, Giot L, Kumar AM, Nandabalan K, Li Y, et al. The Chediak-Higashi protein interacts with SNARE complex and signal transduction proteins. Mol Med. 2002; 8(1):56–64. PMID: 11984006; PubMed Central PMCID: PMC2039936.

24. Hammel I, Lagunoff D, Galli SJ. Regulation of secretory granule size by the precise generation and fusion of unit granules. J Cell Mol Med. 2010; 14(7):1904–16. https://doi.org/10.1111/j.1582-4934.2010.01071.x PMID: 20406331; PubMed Central PMCID: PMC2909340.

25. Rahman M, Haberman A, Tracy C, Ray S, Kramer H. Drosophila mauve mutants reveal a role of LYST homologs late in the maturation of phagosomes and autophagosomes. Traffic. 2012; 13(12):1680–92. https://doi.org/10.1111/tra.12005 PMID: 22934826; PubMed Central PMCID: PMC3528838.

26. Harris E, Wang N, Wu WI WL, Weatherford A, De Lozanne A, Cardelli J. Dictyostelium LvsB mutants model the lysosomal defects associated with Chediak-Higashi syndrome. Mol Biol Cell. 2002; 13 (2):656–69. https://doi.org/10.1091/mbc.01-09-0454 PMID: 11854420; PubMed Central PMCID: PMC65657.

27. Kypri E, Schmauch C, Maniak M, De Lozanne A. The BEACH protein LvsB is localized on lysosomes and postlysosomes and limits their fusion with early endosomes. Traffic. 2007; 8(6):774–83. https://doi.org/10.1111/j.1600-0854.2007.00567.x PMID: 17488289.

28. Kypri E, Falkenstein K, De Lozanne A. Antagonistic control of lysosomal fusion by Rab14 and the Lyst-related protein LvsB. Traffic. 2013; 14(5):599–609. https://doi.org/10.1111/tra.12058 PMID: 23387437; PubMed Central PMCID: PMC3622840.

29. Charette SJ, Cosson P. A LYST/beige homolog is involved in biogenesis of Dictyostelium secretory lysosomes. J Cell Sci. 2007; 120(Pt 14):2338–43. https://doi.org/10.1242/jcs.009001 PMID: 17606989.

30. Charette SJ, Cosson P. Altered composition and secretion of lysosome-derived compartments in Dictyostelium AP-3 mutant cells. Traffic. 2008; 9(4):588–96. https://doi.org/10.1111/j.1600-0854.2008.00706.x PMID: 18194410.

31. Falkenstein K, De Lozanne A. Dictyostelium LvsB has a regulatory role in endosomal vesicle fusion. J Cell Sci. 2014; 127(Pt 20):4356–67. https://doi.org/10.1242/jcs.138123 PMID: 25086066; PubMed Central PMCID: PMC4197084.

32. Lakkaraju A, Umapathy A, Tan LX, Daniele L, Philp NJ, Boesze-Battaglia K, et al. The cell biology of the retinal pigment epithelium. Prog Retin Eye Res. 2020. Epub 2020/02/28. https://doi.org/10.1016/j.preteyeres.2020.100846 PMID: 32105772.

33. Young RW, Bok D. Participation of the retinal pigment epithelium in the rod outer segment renewal process. J Cell Biol. 1969; 42(2):392–403. https://doi.org/10.1083/jcb.42.2.392 PMID: 5792328; PubMed Central PMCID: PMC2107669.

34. Williams DS, Fisher SK. Prevention of rod disk shedding by detachment from the retinal pigment epithelium. Invest Ophthalmol Vis Sci. 1987; 28(1):184–7. PMID: 3804649.

35. Volland S, Esteve-Rudd J, Hoo J, Yee C, Williams DS. A comparison of some organizational characteristics of the mouse central retina and the human macula. PLoS One. 2015; 10(4):e0125631. https://doi.org/10.1371/journal.pone.0125631 PMID: 25923208; PubMed Central PMCID: PMC4414478.

36. LaVail MM. Rod outer segment disk shedding in rat retina: relationship to cyclic lighting. Science. 1976; 194(4269):1071–4. https://doi.org/10.1126/science.982063 PMID: 982063.

37. LaVail MM. Circadian nature of rod outer segment disc shedding in the rat. Invest Ophthalmol Vis Sci. 1980; 19(4):407–11. PMID: 7358492.

38. Katunuma N, Matsunaga Y, Himeno K, Hayashi Y. Insights into the roles of cathepsins in antigen processing and presentation revealed by specific inhibitors. Biol Chem. 2003; 384(6):883–90. https://doi.org/10.1515/BC.2003.099 PMID: 12887055.

39. Ji X, Liu Y, Hurd R, Wang J, Fitzmaurice B, Nishina PM, et al. Retinal Pigment Epithelium Atrophy 1 (rpea1): A New Mouse Model With Retinal Detachment Caused by a Disruption of Protein Kinase C,

theta. Invest Ophthalmol Vis Sci. 2016; 57(3):877–88. https://doi.org/10.1167/iovs.15-17495 PMID: 26978024; PubMed Central PMCID: PMC4794085.

40. Sundberg J, Dawnalyn B, Bechtold L. Ultrastructural Evaluation of Mouse Mutations. In: Sundberg JP, Dawnalyn B, editors. Systematic Approach to Evaluation of Mouse Mutations. Boca Raton, FL: CRC Press; 2000.

41. Fairfield H, Srivastava A, Ananda G, Liu R, Kircher M, Lakshminarayana A, et al. Exome sequencing reveals pathogenic mutations in 91 strains of mice with Mendelian disorders. Genome Res. 2015; 25 (7):948–57. https://doi.org/10.1101/gr.186882.114 PMID: 25917818; PubMed Central PMCID: PMC4484392.

42. Nandrot EF, Anand M, Sircar M, Finnemann SC. Novel role for alphavbeta5-integrin in retinal adhesion and its diurnal peak. Am J Physiol Cell Physiol. 2006; 290(4):C1256–62. https://doi.org/10.1152/ajpcell.00480.2005 PMID: 16338970; PubMed Central PMCID: PMC3237192.

43. Gibbs D, Kitamoto J, Williams DS. Abnormal phagocytosis by retinal pigmented epithelium that lacks myosin VIIa, the Usher syndrome 1B protein. Proc Natl Acad Sci U S A. 2003; 100(11):6481–6. https://doi.org/10.1073/pnas.1130432100 PMID: 12743369; PubMed Central PMCID: PMC164472.

44. Alloatti A, Kotsias F, Pauwels AM, Carpier JM, Jouve M, Timmerman E, et al. Toll-like Receptor 4 Engagement on Dendritic Cells Restrains Phago-Lysosome Fusion and Promotes Cross-Presentation of Antigens. Immunity. 2015; 43(6):1087–100. https://doi.org/10.1016/j.immuni.2015.11.006 PMID: 26682983.

45. Durchfort N, Verhoef S, Vaughn MB, Shrestha R, Adam D, Kaplan J, et al. The enlarged lysosomes in beige j cells result from decreased lysosome fission and not increased lysosome fusion. Traffic. 2012; 13(1):108–19. https://doi.org/10.1111/j.1600-0854.2011.01300.x PMID: 21985295; PubMed Central PMCID: PMC3237799.

46. Huynh C, Roth D, Ward DM, Kaplan J, Andrews NW. Defective lysosomal exocytosis and plasma membrane repair in Chediak-Higashi/beige cells. Proc Natl Acad Sci U S A. 2004; 101(48):16795–800. https://doi.org/10.1073/pnas.0405905101 PMID: 15557559; PubMed Central PMCID: PMC534728.

47. Vilaplana F, Muinos SJ, Nadal J, Elizalde J, Mojal S. Stickler syndrome. Epidemiology of retinal detachment. Arch Soc Esp Oftalmol. 2015; 90(6):264–8. https://doi.org/10.1016/j.oftal.2014.11.001 PMID: 25817961.

48. Vigil-De Gracia P, Ortega-Paz L. Retinal detachment in association with pre-eclampsia, eclampsia, and HELLP syndrome. Int J Gynaecol Obstet. 2011; 114(3):223–5. https://doi.org/10.1016/j.ijgo.2011.04.003 PMID: 21719013.

49. Holden B, Sankaridurg P, Smith E, Aller T, Jong M, He M. Myopia, an underrated global challenge to vision: where the current data takes us on myopia control. Eye (Lond). 2014; 28(2):142–6. https://doi.org/10.1038/eye.2013.256 PMID: 24357836; PubMed Central PMCID: PMC3930268.

50. Saint-Geniez M, D'Amore PA. Development and pathology of the hyaloid, choroidal and retinal vasculature. Int J Dev Biol. 2004; 48(8–9):1045–58. https://doi.org/10.1387/ijdb.041895ms PMID: 15558494.

51. Nentwich MM, Ulbig MW. Diabetic retinopathy—ocular complications of diabetes mellitus. World J Diabetes. 2015; 6(3):489–99. https://doi.org/10.4239/wjd.v6.i3.489 PMID: 25897358; PubMed Central PMCID: PMC4398904.

52. Yagi F, Takagi S, Tomita G. Incidence and causes of iatrogenic retinal breaks in idiopathic macular hole and epiretinal membrane. Semin Ophthalmol. 2014; 29(2):66–9. https://doi.org/10.3109/08820538.2012.760627 PMID: 24409946.

53. Premzl A, Zavasnik-Bergant V, Turk V, Kos J. Intracellular and extracellular cathepsin B facilitate invasion of MCF-10A neoT cells through reconstituted extracellular matrix in vitro. Exp Cell Res. 2003; 283 (2):206–14. https://doi.org/10.1016/s0014-4827(02)00055-1 PMID: 12581740.

54. Porter K, Lin Y, Liton PB. Cathepsin B is up-regulated and mediates extracellular matrix degradation in trabecular meshwork cells following phagocytic challenge. PLoS One. 2013; 8(7):e68668. https://doi.org/10.1371/journal.pone.0068668 PMID: 23844232; PubMed Central PMCID: PMC3700899.

55. Jordans S, Jenko-Kokalj S, Kuhl NM, Tedelind S, Sendt W, Bromme D, et al. Monitoring compartment-specific substrate cleavage by cathepsins B, K, L, and S at physiological pH and redox conditions. BMC Biochem. 2009; 10:23. https://doi.org/10.1186/1471-2091-10-23 PMID: 19772638; PubMed Central PMCID: PMC2759951.

56. Buck MR, Karustis DG, Day NA, Honn KV, Sloane BF. Degradation of extracellular-matrix proteins by human cathepsin B from normal and tumour tissues. Biochem J. 1992; 282 (Pt 1):273–8. PubMed Central PMCID: PMC1130919.

57. Trantow CM, Cuffy TL, Fingert JH, Kuehn MH, Anderson MG. Microarray analysis of iris gene expression in mice with mutations influencing pigmentation. Invest Ophthalmol Vis Sci. 2011; 52(1):237–48. PubMed Central PMCID: PMC3053276. https://doi.org/10.1167/iovs.10-5479 PMID: 20739468

58. Alizadeh P, Smit-McBride Z, Oltjen SL, Hjelmeland LM. Regulation of cysteine cathepsin expression by oxidative stress in the retinal pigment epithelium/choroid of the mouse. Exp Eye Res. 2006; 83(3):679–87. https://doi.org/10.1016/j.exer.2006.03.009 PMID: 16684524; PubMed Central PMCID: PMC1661778.

59. Vidak E, Javorsek U, Vizovisek M, Turk B. Cysteine Cathepsins and their Extracellular Roles: Shaping the Microenvironment. Cells. 2019; 8(3). https://doi.org/10.3390/cells8030264 PMID: 30897858; PubMed Central PMCID: PMC6468544.

60. Aggarwal N, Sloane BF. Cathepsin B: multiple roles in cancer. Proteomics Clin Appl. 2014; 8(5–6):427–37. https://doi.org/10.1002/prca.201300105 PMID: 24677670; PubMed Central PMCID: PMC4205946.

61. Alge-Priglinger CS, Kreutzer T, Obholzer K, Wolf A, Mempel M, Kernt M, et al. Oxidative stress-mediated induction of MMP-1 and MMP-3 in human RPE cells. Invest Ophthalmol Vis Sci. 2009; 50 (11):5495–503. https://doi.org/10.1167/iovs.08-3193 PMID: 19516002.

62. Lu Y, Wahl LM. Oxidative stress augments the production of matrix metalloproteinase-1, cyclooxygenase-2, and prostaglandin E2 through enhancement of NF-kappa B activity in lipopolysaccharide-activated human primary monocytes. J Immunol. 2005; 175(8):5423–9. https://doi.org/10.4049/jimmunol.175.8.5423 PMID: 16210649.

63. Ali MA, Schulz R. Activation of MMP-2 as a key event in oxidative stress injury to the heart. Front Biosci (Landmark Ed). 2009; 14:699–716. https://doi.org/10.2741/3274 PMID: 19273096.

64. Gencer S, Cebeci A, Irmak-Yazicioglu MB. Matrix metalloproteinase gene expressions might be oxidative stress targets in gastric cancer cell lines. Chin J Cancer Res. 2013; 25(3):322–33. https://doi.org/10.3978/j.issn.1000-9604.2013.06.05 PMID: 23825909; PubMed Central PMCID: PMC3696711.

65. Boulton M, McKechnie NM, Breda J, Bayly M, Marshall J. The formation of autofluorescent granules in cultured human RPE. Invest Ophthalmol Vis Sci. 1989; 30(1):82–9. PMID: 2912915.

66. Tate DJ Jr., Miceli MV, Newsome DA. Phagocytosis and H2O2 induce catalase and metallothionein gene expression in human retinal pigment epithelial cells. Invest Ophthalmol Vis Sci. 1995; 36(7):1271–9. PMID: 7775104.

67. Miceli MV, Liles MR, Newsome DA. Evaluation of oxidative processes in human pigment epithelial cells associated with retinal outer segment phagocytosis. Exp Cell Res. 1994; 214(1):242–9. https://doi.org/10.1006/excr.1994.1254 PMID: 8082727.

68. Jiang M, Esteve-Rudd J, Lopes VS, Diemer T, Lillo C, Rump A, et al. Microtubule motors transport phagosomes in the RPE, and lack of KLC1 leads to AMD-like pathogenesis. J Cell Biol. 2015; 210(4):595–611. https://doi.org/10.1083/jcb.201410112 PMID: 26261180; PubMed Central PMCID: PMC4539993.

69. Esteve-Rudd J, Hazim RA, Diemer T, Paniagua AE, Volland S, Umapathy A, et al. Defective phagosome motility and degradation in cell nonautonomous RPE pathogenesis of a dominant macular degeneration. Proc Natl Acad Sci U S A. 2018; 115(21):5468–73. https://doi.org/10.1073/pnas.1709211115 PMID: 29735674; PubMed Central PMCID: PMC6003516.

70. Olsen TW, Chang TS, Sternberg PS. Retinal Detachments Associated with Blunt Trauma. Seminars in Ophthalmology. 2009; 10(1):17–27. https://doi.org/10.3109/08820539509059976 PMID: 10155695.

71. Gonzales CR, Singh S, Yu F, Kreiger AE, Gupta A, Schwartz SD. Pediatric rhegmatogenous retinal detachment: clinical features and surgical outcomes. Retina. 2008; 28(6):847–52. https://doi.org/10.1097/IAE.0b013e3181679f79 PMID: 18536601.

72. Draeger J, Dupuis H. Mechanical factors contributing to the cause of retinal detachment (author's transl). Klin Monbl Augenheilkd. 1975; 166(4):431–5. PMID: 1206914.

73. Zeng R, Zhang Y, Shi F, Kong F. A novel experimental mouse model of retinal detachment: complete functional and histologic recovery of the retina. Invest Ophthalmol Vis Sci. 2012; 53(3):1685–95. https://doi.org/10.1167/iovs.11-8241 PMID: 22323470.

74. Finckh U, von der Kammer H, Velden J, Michel T, Andresen B, Deng A, et al. Genetic association of a cystatin C gene polymorphism with late-onset Alzheimer disease. Arch Neurol. 2000; 57(11):1579–83. https://doi.org/10.1001/archneur.57.11.1579 PMID: 11074789.

75. Lin C, Wang ST, Wu CW, Chuo LJ, Kuo YM. The association of a cystatin C gene polymorphism with late-onset Alzheimer's disease and vascular dementia. Chin J Physiol. 2003; 46(3):111–5. PMID: 14672279.

76. Paraoan L, Grierson I, Maden BE. Fate of cystatin C lacking the leader sequence in RPE cells. Exp Eye Res. 2003; 76(6):753–6. https://doi.org/10.1016/s0014-4835(03)00061-7 PMID: 12742358.